

FUTR3D: A Unified Sensor Fusion Framework for 3D Detection

Xuanyao Chen *

Fudan University

xuanyaochen19@fudan.edu.cn

Tianyuan Zhang *

Carnegie Mellon University

tianyuaz@andrew.cmu.edu

Yue Wang

Massachusetts Institute of Technology

yuewang@csail.mit.edu

Yilun Wang

Li Auto

yilunw@cs.stanford.edu

Hang Zhao †

IIIS, Tsinghua University

Shanghai Qi Zhi Institute

hangzhao@mail.tsinghua.edu.cn

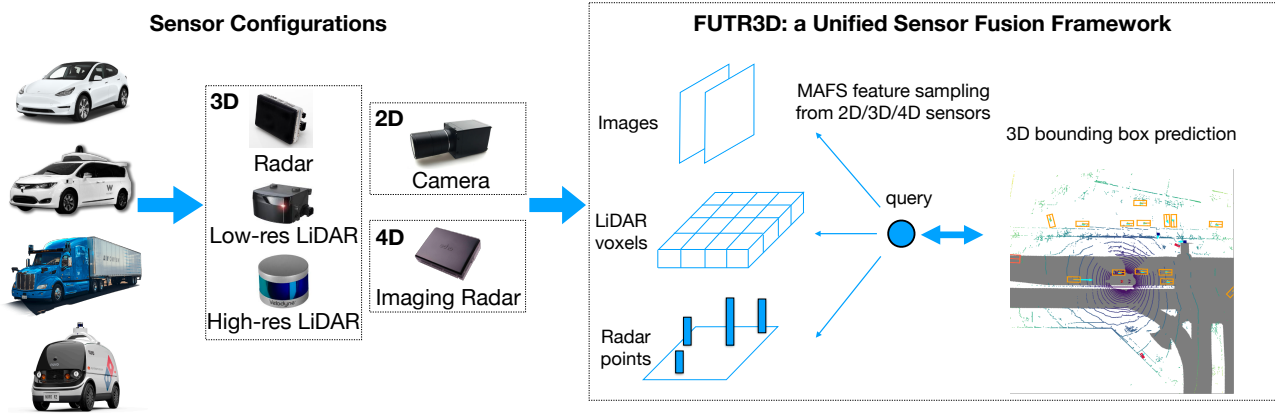


Figure 1. Different self-driving cars have different sensor combinations and setups. FUTR3D is a unified end-to-end sensor fusion framework for 3D detection, which can be used in any sensor configuration, including 2D cameras, 3D LiDARs, 3D radars and 4D imaging radars.

Abstract

Sensor fusion is an essential topic in many perception systems, such as autonomous driving and robotics. Existing multi-modal 3D detection models usually involve customized designs depending on the sensor combinations or setups. In this work, we propose the first unified end-to-end sensor fusion framework for 3D detection, named FUTR3D, which can be used in (almost) any sensor configuration. FUTR3D employs a query-based Modality-

Agnostic Feature Sampler (MAFS), together with a transformer decoder with a set-to-set loss for 3D detection, thus avoiding using late fusion heuristics and post-processing tricks. We validate the effectiveness of our framework on various combinations of cameras, low-resolution LiDARs, high-resolution LiDARs, and Radars. On NuScenes dataset, FUTR3D achieves better performance over specifically designed methods across different sensor combinations. Moreover, FUTR3D achieves great flexibility with different sensor configurations and enables low-cost autonomous driving. For example, only using a 4-beam LiDAR with cameras, FUTR3D (56.8 mAP) achieves on par

*Equal contribution, work done at Shanghai Qi Zhi Institute.

†Corresponding author.

performance with state-of-the-art 3D detection model [38] (56.6 mAP) using a 32-beam LiDAR.

1. Introduction

Sensor fusion is the process of integrating sensory data from disparate information sources. It is an integral part of autonomous perception systems, such as autonomous driving, internet of things, and robotics. With the complementary information captured by different sensors, fusion helps to reduce the uncertainty of state estimation and make more comprehensive and accurate predictions. For instance, on a self-driving car, LiDARs can effectively detect and localize obstacles, while cameras are more capable of recognizing the types of obstacles.

However, multi-sensory systems often come with diverse sensor setups. As shown in Fig. 1, each self-driving car system has a proprietary sensor configuration and placement design. For example, a robo-taxi [1, 5, 25] normally has a 360-degree LiDAR and surround-view cameras on the top, together with perimeter LiDARs or radars around the vehicle; a robo-truck usually has two or more LiDARs on the trailer head, together with long focal length cameras for long-range perception; a passenger car relies on cameras and radars around the vehicle to perform driving assistance. Customizing specialized algorithms for different sensor configurations requires huge engineering efforts. Therefore, designing a unified and effective sensor fusion framework is of great value.

Previous research works have proposed several sophisticated designs for LiDAR and camera fusion. Proposal-based methods either propose bounding boxes from the LiDAR point clouds and then extract corresponding features from camera images [6, 11], or propose frustums from the images and further refine bounding boxes according to point clouds in the frustums [21]. Feature projection-based methods [16, 36] associate modalities by either projecting point features onto the image feature maps, or painting the point clouds with colors [27]. Conducting camera-radar fusion usually involves more complicated feature alignment techniques due to the sparsity of radar signals [3, 10, 18, 19].

Our work introduces the first end-to-end 3D detection framework, named FUTR3D (**F**usion **T**ransformer for **3D** **D**etection), that can work with any sensor setups and combinations, *e.g.* camera-LiDAR fusion, camera-radar fusion, camera-LiDAR-radar fusion. FUTR3D first encodes features for each modality individually, and then employs a query-based Modality-Agnostic Feature Sampler (MAFS) that works in a unified domain and extract features from different modalities. Finally, a transformer decoder operates on a set of 3D queries and performs set predictions of objects. The design of MAFS and transformer decoder makes the model end-to-end and inherently modality agnostic.

The contributions of our work are the following:

- To the best of our knowledge, FUTR3D is the first unified sensor fusion framework that can work with any sensor configuration in an end-to-end manner.
- We design a Modality-Agnostic Feature Sampler, called MAFS. Using 3D queries, MAFS samples and aggregates features from cameras, high-resolution LiDARs, low-resolution LiDARs, and radars. MAFS enables our method to operate on any sensors and their combinations in a modality agnostic way. This module is potentially applicable to any multi-modal use cases.
- FUTR3D outperforms specifically designed fusion methods across different sensor combinations. For example, FUTR3D achieves better performance than PointPainting [27] without bells and whistles.
- FUTR3D achieves excellent flexibility with different sensor configurations and enables low-cost perception systems for autonomous driving. On the nuScenes [1] dataset, FUTR3D achieves 56.8 mAP with a 4-beam LiDAR and camera images, which is on a par with the state-of-the-art model using a 32-beam LiDAR.

2. Related Work

2.1. LiDAR-based 3D Detection

The mainstreams of LiDAR-based detectors in autonomous driving quantify the 3D space into voxels or pillars, then use convolutional backbones to extract a stack of Bird’s-eye view feature maps [13, 37, 38, 42]. Detectors within this framework draw lots of experiences from 2D detector designs. Besides voxel representations, point-based [22, 23], and range view [4, 8, 14, 26] are also explored. PointNet architecture has been used in VoxelNet [42], Lidar-RCNN [15] to extract feature for a small region of irregular points. Several works [8, 14] demonstrate the computational efficiency of Range view. MVF [41] and Pillar-OD [31] introduce multi-view projection to learn view-complementary features. Object DGCNN [33] models object relations using DGCNN [34] and presents the first set prediction based 3D object detection pipeline.

2.2. Camera-based 3D Detection

Directly migrated from 2D object detection, Monodis [24] learns a single-stage 3D object detector on monocular images. FCOS3D [28] considers 3D object detection on multi-view images. It predicts 3D bounding box per image and aggregates predictions in a post-processing step. Pseudo Lidar [30] lifts images into the 3D space and employs a point cloud based pipeline to perform 3D detection. DETR3D [32] designs a set-based 3D object detection model which operates on multi-view images. DETR3D uses camera transformation to link 2D feature extraction to 3D predictions. Also, it does

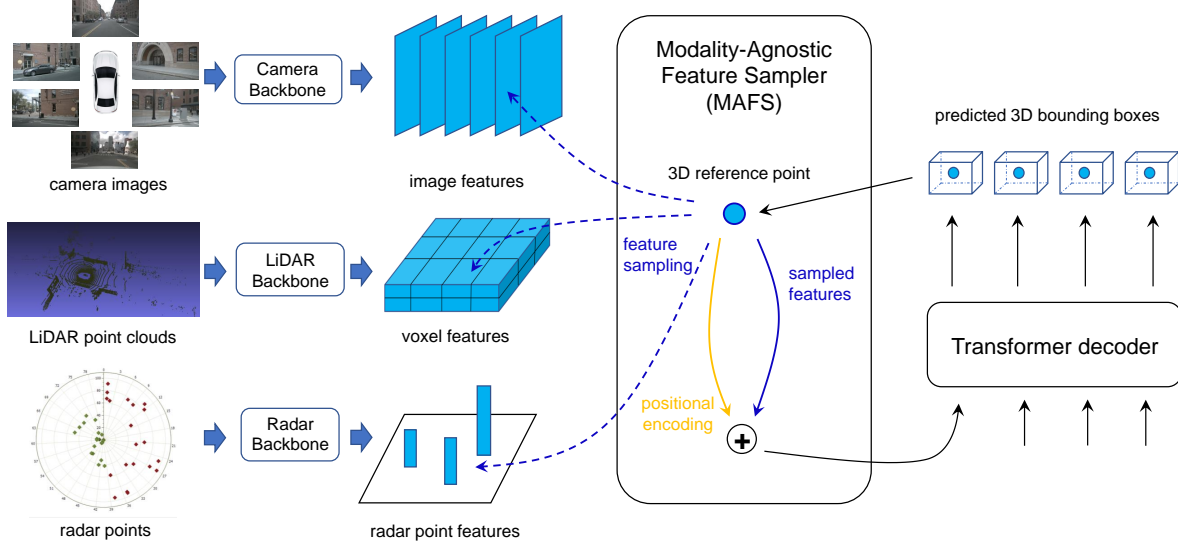


Figure 2. Overview of FUTR3D. Each sensor modality is encoded individually in its own coordinate using modality-specific feature encoder. Then a query-based Modality-Agnostic Feature Sampler (MAFS) extracts features from all available modalities according to the 3D reference point of each query. Finally a transformer decoder predicts 3D bounding boxes from queries. The predicted boxes can be iteratively fed back into MAFS and transformer decoder to refine the predictions.

not require post-processing, thanks to the set prediction module. Our method is closely related to DETR3D in the sense that we use a similar object detection head and feature sampling modules. In contrast to DETR3D, our feature sampling module is *modality agnostic* which makes it work for sensor fusion.

2.3. Multi-modal 3D Detection

Apart from classical heuristic late fusion techniques, we can roughly divide learning-based multi-modal fusion methods into two types: proposal-based methods and feature projection-based methods.

Proposal-based methods have gained a lot of popularity in the past few years. The idea behind such methods is to propose objects from one sensor modality, and then refine it on the other(s). MV3D [6] first generates 3D object proposals in bird’s eye view using LiDAR features, and then projects them to camera view and LiDAR front view to fuse LiDAR camera features. Frustum-PointNet [21] and Frustum-ConvNet [35] use 2D object detectors to generate 2D proposals in the camera view, then lift 2D proposals to 3D frustums, and finally use perform 3D box estimation within the frustums. AVOD [11] places dense anchor boxes in bird’s eye view and then projects these anchors to camera images and LiDAR voxels for feature fusion and region proposal.

Feature projection-based methods usually perform feature projection and fusion before the detection head. By finding the point-pixel correspondence, [36] enables middle-level feature fusion, and makes a single-stage detector. Cont-

Fuse [16] further uses a KNN to better find matching points for image pixels, and fuses features at multiple levels. The top-performing camera-LiDAR based 3D detection algorithm PointPaint [27] projects LiDAR points onto the prediction map of a pre-trained image semantic segmentation network, and fuse the semantic prediction label with the intensity measurement of each point. MVP [39] generate dense virtual points with semantic label to make more use of image information. Although feature projection-based methods have recently achieved impressive performance, their designs usually require a lot of heuristics and understanding of the sensor modalities.

There are also a handful of works on fusing camera images and radar signals that share similar spirits with camera-LiDAR fusion. [3, 10, 19] encode both camera images and radar signals in the perspective view and fuse them by simple feature map concatenation. CenterFusion [18] proposes 3D bounding boxes from images, and further refines them by fusing their features with radar signals in the bird’s eye view representations.

3. Approach

FUTR3D can be conceptually divided into four parts. First, the data from different sensor modalities are encoded by their modality-specific feature encoders (§3.1). Then, a query-based Modality Agnostic Feature Sampler (MAFS) is used to sample and aggregate features from all modalities, according to the initial positions of the queries (§3.2); this is the major novelty of this work. Next, a shared transformer decoder head is used to refine the bounding box pre-

dictionaries based on the fused features using an iterative refinement module (§3.3). Finally, our loss is based on set-to-set matching between predictions and ground-truths (§3.4). FUTR3D is designed to be a unified framework for *multi-modal* sensor fusion, which makes single-modal methods like DETR3D [32] and Object DGCNN [33] special cases of our method. An overview of FUTR3D is shown in Figure 2.

3.1. Modality-specific Feature Encoding

FUTR3D encodes features of each modality independently. Since our framework does not make assumptions about the modalities used or their model architectures, our model works with *any* choices of feature encoders. This work focuses on three types of data: LiDAR point clouds, Radar point clouds, and multi-view camera images.

For LiDAR point clouds, we use a VoxelNet [37, 42] with 0.1m voxel size or PointPillar [13] with 0.2m pillar size to encode LiDAR point clouds. After 3D backbone and FPN [17], we obtain multi-scale Bird’s-eye view (BEV) feature maps $\{\mathcal{F}_{\text{lid}}^j \in \mathbb{R}^{C \times H_j \times W_j}\}_{j=1}^M$, where M is the number of feature levels output from FPN.

We consider N Radar points $\{r_j\}_{j=1}^N \in \mathbb{R}^{C_{\text{rad}}}$ where C_{rad} denotes the number of features of the radar points, such as location, speed and intensity. We adopt a shared MLP Φ_{rad} to obtain per-point features $\mathcal{F}_{\text{rad}}^j = \Phi_{\text{rad}}(r_j) \in \mathbb{R}^C$.

On a typical self-driving car, we have O surrounding cameras. Following prior works [27, 28, 32, 38], we use ResNet [9] and FPN [17] for image feature extraction, it outputs multi-scale features for each image, denoted as $\mathcal{F}_{\text{cam}}^o = \{\mathcal{F}_{\text{cam}}^{oj} \in \mathbb{R}^{C \times H_j \times W_j}\}_{j=1}^M$ for the o -th camera image.

3.2. Modality-Agnostic Feature Sampler

The most critical part of FUTR3D is the feature sampling process, termed Modality-Agnostic Feature Sampler (MAFS). The input of our detection head is a set of object queries $Q = \{q_i\}_{i=1}^{N_q} \subset \mathbb{R}^C$, and features from different sensors. MAFS updates each query by sampling features from feature maps of each sensor and fusing them.

Initial 3D reference points. As the first step, MAFS decodes a 3D reference point from each object query by a linear transformation and sigmoid normalization

$$c_i = \Phi_{\text{ref}}(q_i), \quad (1)$$

where $c_i \in [0, 1]^3$ presents relative coordinates in 3D space. Then, this 3D reference point serves as an anchor to gather features from multiple sources. The initial reference point does not depend on features from any sensors, and it will be refined dynamically after fusing features from all modalities.

LiDAR feature sampling. The point cloud features after the 3D backbone and FPN [17] are denoted as $\{\mathcal{F}_{\text{lid}}^j\}_{j=1}^M$. We use $\mathcal{P}(c_i)$ to denote the projection of the 3D reference point in the BEV. We sample LiDAR features from all multi-scale BEV feature maps and sum them:

$$\mathcal{SF}_{\text{lid}}^i = \sum_{j=1}^M \mathcal{F}_{\text{lid}}^j(\mathcal{P}(c_i)) \cdot \sigma_{\text{lid}}^{ij}, \quad (2)$$

where $\mathcal{SF}_{\text{lid}}^i$ means the sampled LiDAR features for i -th reference point, $\mathcal{F}_{\text{lid}}^j(\mathcal{P}(c_i))$ represents the bilinear sampling from the BEV feature map, and the weighting factor $\{\sigma_{\text{lid}}^{ij}\}_{j=1}^M = \phi_{\text{lid}}(q_i)$ is computed per query by a linear transformation and sigmoid normalization.

Radar feature sampling. In the Radar point clouds, we pick top- K nearest Radar points $\{r_1, r_2, \dots, r_K\}$ for each object query, according to its 3D reference point. Their features $\{\mathcal{F}_{\text{rad}}^j\}_{j=1}^K$ are sampled by taking a weighted sum as

$$\mathcal{SF}_{\text{rad}}^i = \sum_{j=1}^K \mathcal{F}_{\text{rad}}^j \cdot \sigma_{\text{rad}}^{ij} \quad (3)$$

where $\{\sigma_{\text{rad}}^{ij}\}_{j=1}^K = \phi_{\text{rad}}(q_i)$ is a weighting factor predicted per reference point by linearly projecting object query q_i and sigmoid normalization.

Image feature sampling. We project the reference point c_i to the image of o -th camera by utilizing the camera’s intrinsic and extrinsic parameters and denote the coordinates of the projected reference point as $\mathcal{T}_o(c_i)$.

We use the projected image coordinates $\mathcal{T}_o(c_i)$ to sample point features from feature maps of all cameras, and perform weighted sum

$$\mathcal{SF}_{\text{cam}}^i = \sum_{o=1}^O \sum_{j=1}^M \mathcal{F}_{\text{cam}}^{oj}(\mathcal{T}_o(c_i)) \cdot \sigma_{\text{cam}}^{ijo} \quad (4)$$

where $\mathcal{F}_{\text{cam}}^{oj}(\mathcal{T}_o(c_i))$ denotes the bilinear sampling using the image coordinates. If the projected point’s coordinate $\mathcal{T}_o(c_i)$ is out of the o -th image plane, we set the sampled value to be zero. Then scalar weight $\sigma_{\text{cam}}^{ijo}$ is also decoded from object query q_i using a linear layer and sigmoid normalization.

Modality-agnostic feature fusion. Our insight is that object attributes are not equally recognizable in different modalities. Therefore, we seek to take advantage of different modalities and extract complementary information from them. After sampling point features from all modalities, we fuse features and update queries. First, we concatenate sampled features from all modalities and encode them using a MLP network Φ_{fus} given by

$$\mathcal{SF}_{\text{fus}}^i = \Phi_{\text{fus}}(\mathcal{SF}_{\text{lid}}^i \oplus \mathcal{SF}_{\text{cam}}^i \oplus \mathcal{SF}_{\text{rad}}^i), \quad (5)$$

where $\mathcal{SF}_{\text{fus}}^i$ is the fused features per query. Then, we add the positional encoding of reference points to the fused features to make them location aware. Finally, we update the queries accordingly by $q_i = q_i + \Delta q_i$, where

$$\Delta q_i = \mathcal{SF}_{\text{fus}}^i + \text{PE}(c_i). \quad (6)$$

We also use self-attention modules to let object queries interact with each other, where the query, keys, values are all the object queries. The skip connection is implemented following DETR [2], where

$$Q = Q + \text{SelfAttn}(Q). \quad (7)$$

Thanks to this modality agnostic feature fusion module, our method works with any sensor combinations. We use the same object detection head throughout.

3.3. Iterative 3D Box Refinement

Each block $\ell \in \{1, 2, \dots, L\}$ of transformer decoder in our detection head produces a set of updated object queries $Q^\ell = \{q_i^\ell\}_{i=1}^{N_q} \subset \mathbb{R}^C$. We predict a sequence of iteratively refined boxes given the queries. Specifically, for each object query q_i^ℓ , we use a shared MLP Φ_{reg} to predict offset to box center coordinate $\Delta x_i^\ell \in \mathbb{R}^3$, box size $(w_i^\ell, h_i^\ell, l_i^\ell)$, orientation $(\sin \theta_i^\ell, \cos \theta_i^\ell)$, velocity $(v_i^\ell \in \mathbb{R}^2)$ and another Φ_{cls} for its categorical label \hat{y}_i^ℓ .

Following [32, 33, 44], we adopt an iterative refinement approach. We use the predictions of box center coordinates in the last layer as the 3D reference points for each query, except for the first layer which directly decoding the object queries like eq. 1 as input. The next layer’s reference points are given by

$$c_i^{\ell+1} = c_i^\ell + \Delta x_i^\ell. \quad (8)$$

3.4. Loss

Following [2, 32, 33, 44], we compute a set-to-set loss between predictions and ground-truths, which involves two steps: First, we perform one-to-one matching between predictions and ground-truth boxes using bipartite matching. Then, we compute both the regression loss and the classification loss given the one-to-one matching. In particular, the one-to-one assignment problem can be solved by the Hungarian algorithm [12].

4. Experiments

4.1. Implementation Details

Dataset. We use nuScenes [1] dataset for all experiments. This dataset consists of 3 modalities, namely 6 cameras, 5 radars and 1 LiDAR. All are captured with a full 360-degree field of view. There are totally 1000 sequences, where each sequence has roughly 40 annotated keyframes.

The keyframes are synchronized across sensors with a sampling rate of 2 FPS.

Cameras. In each frame, nuScenes [1] provides images from six cameras [front_left, front, front_right, back_left, back, back_right]; there are overlap regions between cameras and the whole scene is covered. The resolution is 1600×900 .

LiDAR. nuScenes provides a 32-beam LiDAR, which spins at 20 FPS. For point clouds, we set the detection range to $[-51.2m, 51.2m]$ for the X and Y axis, and $[-5m, 3m]$ for the Z axis. Since only key frames are annotated at 2 FPS, we follow the common practice to transform points from the past 9 frames to the current frame.

Low-resolution LiDAR. Low-resolution LiDARs are often used in many low cost uses cases. We consider these low-resolution LiDARs as complementary setups to high-resolution LiDARs because they are scalable to be deployed on production-ready platforms. We simulate low-resolution LiDAR outputs from the 32-beam LiDAR. We first convert points from Cartesian coordinate system to spherical coordinates: range r , inclination θ , and azimuth ϕ . The range of inclination is $[-30^\circ, 10^\circ]$ For 4-beam LiDAR, we select beams whose inclination θ fall within $[-7.1^\circ, -5.8^\circ] \cup [-4.5^\circ, -3.2^\circ] \cup [-1.9^\circ, -0.6^\circ] \cup [0.7^\circ, 2.0^\circ]$. For 1-beam LiDAR, we select the beam with pitch angle in $[-1.9^\circ, -0.6^\circ]$.

Radar. We stack points captured by all five Radars into a single point cloud; each point cloud contains 200 to 300 points per frame. We use point coordinates, velocity measurements and intensities as Radar features.

Model setting. The feature dimension C is all 256 for LiDAR feature \mathcal{F}_{lid} , image feature \mathcal{F}_{cam} , object queries Q . In LiDAR and image feature extraction, we use $M = 4$ layers of multi-scale features encoded by FPN. As for Radar features, we pick $K = 10$ nearest points when sampling. There is total $L = 6$ blocks in transformer decoder of detection head.

Training details. For LiDAR-based detectors, we follow training schedules from prior works [33, 37, 38, 43]. We extended the training schedules from 20 epochs to 38 epochs; then we removed the object sampling augmentation [37, 38] at the last 2 epochs. For LiDAR-camera models, we pre-train the LiDAR backbone and the camera backbone respectively, then jointly fine-tune the model. For camera-radar models, we pre-train the image model, followed by a jointly training on cameras and radars.

Evaluation metrics. Mean Average Precision (mAP) and nuScenes Detection Score (NDS) are the major metrics for the nuScenes 3D detection benchmark. For mAP, nuScenes considers the distances between centers of the bounding boxes on bird’s eye view. NDS measures the quality of detection results by consolidating several breakdown

Table 1. **Camera-LiDAR fusion results.** FUTR3D outperforms state-of-the-art model PointPainting under all different configurations of LiDAR and cameras on the nuScenes validation set. Under camera + 4-beam LiDAR setting with pretraining, FUTR3D achieves 56.8 mAP, which is on par with state-of-the-art LiDAR detector CenterPoint-Voxel with 32-beam LiDAR (56.6 mAP). We use VoxelNet with 0.1 meter voxel size as point cloud backbone for all methods.

	NDS \uparrow	mAP \uparrow	mATE \downarrow	mASE \downarrow	mAOE \downarrow	mAVE \downarrow	mAAE \downarrow
32-beam LiDAR + Camera							
PointPainting [27]	67.8	62.8	29.6	25.5	32.5	29.3	19.0
FUTR3D	68.0	64.2	35.0	25.9	30.4	30.5	19.3
4-beam LiDAR + Camera							
PointPainting [27]	59.4	50.0	34.4	26.6	44.3	32.6	18.4
FUTR3D	61.5	54.9	43.4	26.5	35.2	36.8	18.0
FUTR3D + DDAD pretrain [20]	62.9	56.8	41.1	26.3	33.6	35.0	18.6
1-beam LiDAR + Camera							
PointPainting [27]	41.0	22.0	50.3	28.0	62.3	40.0	19.5
FUTR3D	50.0	41.3	61.0	26.9	40.8	59.0	18.7

Table 2. **Single modality results.** Table (a), (b), and (c) list single-modality results on surrounding cameras, 32-beam LiDAR, 4-beam LiDAR and 1-beam LiDAR on nuScenes validation split. All results are obtained without test time augmentation and model ensembles. If not specified, results are obtained by our re-implementation using MMDetection3D [7]. *: from paper PGD [29]. ‡: from MMDetection3D.

(a) Camera			(b) 32-beam LiDAR			(c) Low-resolution LiDAR		
methods	NDS \uparrow	mAP \uparrow	methods	NDS \uparrow	mAP \uparrow	methods	NDS \uparrow	mAP \uparrow
CenterNet* [40]	32.8	30.6	CenterPoint-Pillar ‡	59.7	49.1	4-beam CenterPoint	53.6	38.5
FCOS3D* [28]	41.5	34.3	CenterPoint-Voxel ‡	64.5	56.6	4-beam FUTR3D	54.8	42.1
PGD* [29]	42.8	36.9	FUTR3D-Pillar	60.4	51.3	1-beam CenterPoint	36.9	14.5
FUTR3D	42.5	34.6	FUTR3D-Voxel	65.5	59.3	1-beam FUTR3D	37.9	16.4

metrics: Average Translation Error (ATE), Average Scale Error (ASE), Average Orientation Error (AOE), Average Velocity Error (AVE), and Average Attribute Error (AAE). We average the metrics over all classes, following the official evaluation protocol.

4.2. Multi-modal Detection

We demonstrate the effectiveness of our framework under several sensor combinations.

LiDAR with Cameras is the most commonly used sensor combination for autonomous driving. Here, we consider two types of camera LiDAR combinations: cameras combined with low-resolution LiDAR for low-cost use cases, and cameras combined with high-resolution LiDAR for accurate perception. We simulate 4-beam and 1-beam LiDAR as mentioned in §4.1. We compare our method with state-of-the-art methods PointPainting [27] in these two scenarios in Table 1. For a better understanding of how multi-modality improve over single-modality methods, we list the single-modality results in Table 2a for cameras, Table 2b for high-resolution LiDARs, and Table 2c for low-resolution LiDARs. In the camera-only setting, FUTR3D degenerates to DETR3D [32], and in LiDAR-only setting, FUTR3D degenerates to Object DGCNN [33].

FUTR3D outperforms PointPainting by **1.4** mAP on 32-beam LiDARs plus cameras setting, and **19.7** mAP on 1-beam LiDARs plus cameras setting. PointPainting uses ex-

tra image data from nuImages to pre-train its image segmentation models while our method does not include any additional data.

FUTR3D is able to achieve comparable performance using lower cost sensor configurations. For instance, under the 4-beam LiDAR with cameras setting, FUTR3D reaches 54.9 mAP, which is slightly behind (by 1.7 mAP) one of the top-performing LiDAR detectors, CenterPoint-Voxel [38] with 32-beam LiDAR (56.6 mAP). More importantly, when using DD3D [20] depth pretrained models for our camera backbone, 4-beam LiDAR with cameras outperform 32-beam LiDAR and achieve 56.8 mAP.

When adding cameras to 1-beam LiDAR, PointPainting improves over LiDAR-only CenterPoint only by 7.5 mAP, whereas FUTR3D improves over its LiDAR version by **25.7** mAP. This demonstrates that FUTR3D is more general than PointPainting.

Cameras with Radars is a cheap sensor combination commonly seen in driver-assist system on passenger cars. Radars provide sparse points with depth and velocity information. As is shown in Table 3, we reach comparable results with SOTA method CenterFusion [18]. Besides mAP and NDS metrics, we also report mAVE (mean Average Velocity Error), which is used to measure the error of box velocity predictions. Since the single-frame camera images cannot provide effective cues for velocity predictions, camera-radar combination improves over camera-

only methods on mAVE dramatically.

Table 3. **Camera-radar fusion results.** FUTR3D is on par with state-of-the-art model CenterFusion. Compared to the camera-only model, radar helps to decrease errors of velocity predictions (mAVE).

methods	NDS \uparrow	mAP \uparrow	mAVE \downarrow
CenterFusion [18]	45.3	33.2	0.540
FUTR3D camera-only	42.5	34.6	0.842
FUTR3D	45.9	35.0	0.561

4.3. Characteristics of Cameras and LiDARs

As shown in Section 4.2, FUTR3D is a unified detection framework that can work in camera-only, LiDAR-only and camera-LiDAR fusion settings. To the best of our knowledge, it is the first time one can control for the detection method and study the performance gain of sensor fusion comparing to each sensor respectively. To investigate the characteristics of different sensors, we break down the performance of FUTR3D on different camera-LiDAR combinations by object distances, different sizes and object categories.

Object category. We report Average Precision (AP) of our LiDAR and cameras methods for every object category in Table 4. Though the overall mAP of the 4-beam LiDAR only FUTR3D is higher than the camera-only FUTR3D (42.1 mAP v.s. 34.6 mAP). The camera-only model outperforms the 4-beam LiDAR model on bicycles, traffic cones and barriers, showing that 4-beam LiDAR are not good at detecting small objects. Moreover, when equipping the 4-beam LiDAR with cameras, the performance on bicycles, traffic cones and motorcycles are significantly boosted.

Object distance. We split ground truth boxes into three subsets given the distances of box centers to ego vehicle: $[0m, 20m]$, $[20m, 30m]$, $[30m, +\infty]$, with each group taking up 42.93%, 28.27%, 28.8% of all the ground truth boxes. Note that boxes of `traffic_cone` and `barrier` with distances larger than 30 meters will be automatically filtered out following official evaluation protocols of nuScenes 3D detection. Table 5 shows the results. For boxes farther than 30 meters, our camera-only FUTR3D only achieves 10.4 mAP, when our 4-beam LiDAR model obtains 16.1 mAP. However, fusing these two sensors elevate the performance to the next level (27.4 mAP). Even for the 32-beam LiDAR model, additional camera sensors can improve the performance of our model on farther objects from 29.9 mAP to 36.7 mAP. Adding cameras improves LiDAR perception the most on farther regions.

Object size. We split ground truth boxes into two subsets: $[0m, 4m]$ & $[4m, +\infty]$ based on the longer edge of the 3D box, each group occupying 46.18%, and 53.82% of the gt boxes. Table 6 reports the mAP of our camera LiDAR models on each group. The performance improvements introduced by adding cameras to all LiDAR models

are larger on small objects than on large objects. Cameras improve LiDAR-based detectors more on small objects since cameras have much high resolution than even 32-beam LiDARs. However, the performance improvements introduce by adding different LiDARs to camera-only models are roughly the same for small and large objects, meaning depth information are equally useful when localizing both small and large objects.

4.4. Ablation Study

Object queries. We show the performance of FUTR3D using different number of queries. We report results under LiDAR-only and camera-LiDAR settings. As shown in Table 7, the number of queries in the decoder head only affects the performance slightly. In other experiments, we use 600 queries unless specified.

Backbone choices. We show FUTR3D under different camera-LiDAR backbone combinations in Table 8. For vision backbones, we experiment with ResNet-50 and ResNet-101. For LiDAR backbones, we experiment with PointPillar [13] with 0.2m pillar size and more powerful VoxelNet [42] with 0.1m and 0.075m voxel sizes. We can see that deep vision model and small voxel sizes benefit the final performance. As a trade-off between performance and efficiency, we use ResNet-50 and VoxelNet with 0.1m voxel size as our default setting in other experiments.

4.5. Qualitative Results

In Figure 3, we visualize and compare the results with different settings. In Figure 3a, we show the results of 4-beam LiDAR + cameras (left) and 32-beam LiDAR only (right). Using sparse LiDAR beams and cameras, our method is still able to detect the car in the distance, circled in red, when it is missed using 32-beam LiDAR. Cameras provide denser pixels than LiDAR beams which could be useful for detecting far away objects. In Figure 3b, we show the results of 1-beam LiDAR + cameras (left) and cameras only (right). With the help of only 1-beam LiDAR, camera is able to eliminate the false positive in red circle as LiDAR gives geometry information directly to the model. This validates the effectiveness of FUTR3D framework. Furthermore, this is in line with our assumption that in many cases, low-cost LiDARs and cameras are comparable with expensive LiDARs in object recognition.

4.6. Complexity analysis

In Table 9, we show the number of parameters and FLOPS (number of floating point operations per inference) of each component of our model. We can see that the MAFS sampler and decoder of FUTR3D are lightweight and efficient. The complexity of the model depends on the backbones, where users can make their own choices according to practical system requirement.



(a) 4-beam LiDAR+Cameras vs. 32-beam LiDAR.



(b) 1-beam LiDAR+Cameras vs. Cameras.

Figure 3. Qualitative results of FUTR3D. We show perspective image view results by projecting LiDAR points onto images. (a) There is a car in the distance marked in red circle which can be detected using 4-beam LiDAR with cameras. (b) The billboard circled in red is detected falsely as pedestrian using vision only. This can be corrected with the help of 1-beam LiDAR.

Table 4. Performance breakdown by object categories. Cameras help LiDAR-based detectors significantly on bicycles, traffic cones and motorcycles. Abbreviations: construction vehicle (CV), pedestrian (Ped), motorcycle (Motor), and traffic cone (TC).

modalities	AP									
	Car	Truck	Bus	Trailer	CV	Ped	Motor	Bicycle	TC	Barrier
Camera only	54.3	29.8	36.2	16.7	7.7	41.6	32.9	29.6	51.1	47.6
1-beam LiDAR	29.6	16.0	30.4	13.8	3.3	32.5	6.4	6.0	9.5	22.0
1-beam LiDAR + Camera	61.1	39.7	49.6	22.6	12.6	55.2	39.7	33.1 ↑ 27.1	52.1 ↑ 42.6	47.2
4-beam LiDAR	70.1	39.4	50.5	30.0	12.2	68.6	44.2	17.3	41.0	47.5
4-beam LiDAR + Camera	78.0	54.4	61.5	32.2	20.4	75.7	61.4	53.9 ↑ 36.6	58.1 ↑ 17.1	53.9
32-beam LiDAR	84.3	53.4	65.2	41.6	25.2	81.5	66.4	48.7	64.1	62.6
32-beam LiDAR + Camera	86.3	61.5	71.9	42.1	26.0	82.6	73.6	63.3 ↑ 14.6	70.1 ↑ 6.0	64.4

5. Conclusion

We propose a unified end-to-end sensor fusion framework for 3D object detection. Our insight is that a query-based modality-agnostic feature sampler (MAFS) enables our model to work with any sensor combinations and setups. We hope this architecture can serve as a foundation framework for multi-modal fusion and 3D scene understanding.

References

- [1] Holger Caesar, Varun Bankiti, Alex H Lang, Sourabh Vora, Venice Erin Liong, Qiang Xu, Anush Krishnan, Yu Pan, Giancarlo Baldan, and Oscar Beijbom. nuscenes: A multi-modal dataset for autonomous driving. In *Proceedings of the IEEE/CVF conference on computer vision and pattern recognition*, pages 11621–11631, 2020. 2, 5, 11
- [2] Nicolas Carion, Francisco Massa, Gabriel Synnaeve, Nicolas

Table 5. Performance breakdown by object distance. We split boxes given its ego distance and report mAP independently. Results show **cameras help LiDAR-based detectors more on farther objects**.

	mAP		
	[0m, 20m]	[20m, 30m]	[30m, +∞]
Camera only	49.3	25.4	10.4
4-beam LiDAR	61.1	39.3	16.1
4-beam LiDAR + Camera	69.8 ↑ 8.7	50.5 ↑ 10.2	27.4 ↑ 11.3
32-beam LiDAR	73.8	55.2	29.9
32-beam LiDAR + Camera	76.8 ↑ 3.0	58.8 ↑ 3.6	36.7 ↑ 6.8

Table 6. Performance breakdown by object size. We split the boxes given its longest edge. Results indicate that **cameras improve LiDAR-based detectors more on small objects**.

	mAP	
	[0m, 4m]	[4m, +∞]
Camera only	22.3	13.9
1-beam LiDAR	9.2	8.9
1-beam LiDAR + Camera	25.5 ↑ 16.3	17.8 ↑ 8.9
4-beam LiDAR	25.3	19.4
4-beam LiDAR + Camera	33.9 ↑ 8.6	23.4 ↑ 4.0
32-beam LiADR	36.4	25.7
32-beam LiDAR + Camera	39.5 ↑ 3.1	27.4 ↑ 1.7

Table 7. Ablation on the number of object queries.

# queries	FUTR3D-Voxel		FUTR3D-Voxel+Cam	
	NDS	mAP	NDS	mAP
300	65.4	58.4	67.8	63.3
600	65.5	59.3	68.0	64.2
900	64.0	57.8	67.5	63.5

Table 8. Ablation on encoder backbones.

backbones		NDS ↑	mAP ↑
Vision	LiDAR		
ResNet-50	PointPillar 0.2m	63.3	57.3
ResNet-50	VoxelNet 0.1m	66.3	61.4
ResNet-101	PointPillar 0.2m	65.1	60.3
ResNet-101	VoxelNet 0.1m	68.0	64.2
ResNet-101	VoxelNet 0.075m	68.3	64.5

Table 9. Computation and complexity analysis. The vision backbone’s FLOPS are calculated with 6 surround view images as input and the LiDAR backbone with point clouds accumulated from 10 sweeps.

	#param.	FLOPS
ResNet-50	27.6M	673G
ResNet-101	47.7M	1023G
0.2 PointPillar	5.5M	50G
0.1 VoxelNet	8.3M	44G
sampler & decoder	7.5M	2G

- Usunier, Alexander Kirillov, and Sergey Zagoruyko. End-to-end object detection with transformers. In *ECCV*, 2020. **5**
- [3] Simon Chadwick, Will Maddern, and Paul Newman. Distant vehicle detection using radar and vision. In *2019 International Conference on Robotics and Automation (ICRA)*, pages 8311–8317. IEEE, 2019. **2, 3**
- [4] Yuning Chai, Pei Sun, Jiquan Ngiam, Weiyue Wang, Benjamin Caine, Vijay Vasudevan, Xiao Zhang, and Dragomir Anguelov. To the Point: Efficient 3D Object Detection in the Range Image With Graph Convolution Kernels. In *CVPR*, 2021. **2**
- [5] Ming-Fang Chang, John Lambert, Patsorn Sangkloy, Jagjeet Singh, Slawomir Bak, Andrew Hartnett, De Wang, Peter Carr, Simon Lucey, Deva Ramanan, et al. Argoverse: 3d tracking and forecasting with rich maps. In *Proceedings of the IEEE/CVF Conference on Computer Vision and Pattern Recognition*, pages 8748–8757, 2019. **2**
- [6] Xiaozhi Chen, Huimin Ma, Ji Wan, Bo Li, and Tian Xia. Multi-View 3D Object Detection Network for Autonomous Driving. In *CVPR*, pages 1907–1915, 2017. **2, 3**
- [7] MMDetection3D Contributors. Mmdetection3d: Open-mmlab next-generation platform for general 3d object detection, 2020. **6, 11**
- [8] Lue Fan, Xuan Xiong, Feng Wang, Naiyan Wang, and ZhaoXiang Zhang. RangeDet: In Defense of Range View for LiDAR-Based 3D Object Detection. In *ICCV*, 2021. **2**
- [9] Kaiming He, Xiangyu Zhang, Shaoqing Ren, and Jian Sun. Deep Residual Learning for Image Recognition. In *CVPR*, pages 770–778, 2016. **4**
- [10] Vijay John and Seiichi Mita. Rvnet: Deep sensor fusion of monocular camera and radar for image-based obstacle detection in challenging environments. In *Pacific-Rim Symposium on Image and Video Technology*, pages 351–364. Springer, 2019. **2, 3**
- [11] Jason Ku, Melissa Mozifian, Jungwook Lee, Ali Harakeh, and Steven L Waslander. Joint 3D Proposal Generation and Object Detection from View Aggregation. In *IROS*, pages 1–8. IEEE, 2018. **2, 3**
- [12] Harold W Kuhn. The hungarian method for the assignment problem. *Naval research logistics quarterly*, 2(1-2):83–97, 1955. **5**
- [13] Alex H Lang, Sourabh Vora, Holger Caesar, Lubing Zhou, Jiong Yang, and Oscar Beijbom. PointPillars: Fast Encoders for Object Detection from Point Clouds. In *CVPR*, pages 12697–12705, 2019. **2, 4, 7**
- [14] Bo Li, Tianlei Zhang, and Tian Xia. Vehicle Detection from 3D Lidar Using Fully Convolutional Network. *Robotics: Science and Systems*, 2016. **2**
- [15] Zhichao Li, Feng Wang, and Naiyan Wang. LiDAR R-CNN: An Efficient and Universal 3D Object Detector. In *CVPR*, 2021. **2**
- [16] Ming Liang, Bin Yang, Shenlong Wang, and Raquel Urtasun. Deep Continuous Fusion for Multi-Sensor 3D Object Detection. In *ECCV*, pages 641–656, 2018. **2, 3**
- [17] Tsung-Yi Lin, Piotr Dollár, Ross Girshick, Kaiming He, Bharath Hariharan, and Serge Belongie. Feature Pyramid Networks for Object Detection. In *CVPR*, pages 2117–2125, 2017. **4**

- [18] Ramin Nabati and Hairong Qi. Centerfusion: Center-based radar and camera fusion for 3d object detection. In *Proceedings of the IEEE/CVF Winter Conference on Applications of Computer Vision*, pages 1527–1536, 2021. 2, 3, 6, 7
- [19] Felix Nobis, Maximilian Geisslinger, Markus Weber, Johannes Betz, and Markus Lienkamp. A deep learning-based radar and camera sensor fusion architecture for object detection. In *2019 Sensor Data Fusion: Trends, Solutions, Applications (SDF)*, pages 1–7. IEEE, 2019. 2, 3
- [20] Dennis Park, Rares Ambrus, Vitor Guizilini, Jie Li, and Adrien Gaidon. Is pseudo-lidar needed for monocular 3d object detection? In *Proceedings of the IEEE/CVF International Conference on Computer Vision*, pages 3142–3152, 2021. 6
- [21] Charles R Qi, Wei Liu, Chenxia Wu, Hao Su, and Leonidas J Guibas. Frustum PointNets for 3D Object Detection from RGB-D Data. In *CVPR*, pages 918–927, 2018. 2, 3
- [22] Charles R Qi, Hao Su, Kaichun Mo, and Leonidas J Guibas. PointNet: Deep Learning on Point Sets for 3D Classification and Segmentation. In *CVPR*, pages 652–660, 2017. 2
- [23] Charles Ruizhongtai Qi, Li Yi, Hao Su, and Leonidas J Guibas. PointNet++: Deep Hierarchical Feature Learning on Point Sets in a Metric Space. In *NeurIPS*, pages 5099–5108, 2017. 2
- [24] Andrea Simonelli, Samuel Rota Buló, Lorenzo Porzi, Manuel López-Antequera, and Peter Kotschieder. Disentangling monocular 3d object detection. In *Proceedings of the IEEE/CVF International Conference on Computer Vision*, pages 1991–1999, 2019. 2
- [25] Pei Sun, Henrik Kretzschmar, Xerxes Dotiwalla, Aurelien Chouard, Vijaysai Patnaik, Paul Tsui, James Guo, Yin Zhou, Yuning Chai, Benjamin Caine, et al. Scalability in Perception for Autonomous Driving: Waymo Open Dataset. In *CVPR*, pages 2446–2454, 2020. 2
- [26] Pei Sun, Weiyue Wang, Yuning Chai, Gamaleldin Elsayed, Alex Bewley, Xiao Zhang, Cristian Sminchisescu, and Dragomir Anguelov. Rsn: Range sparse net for efficient, accurate lidar 3d object detection. In *CVPR*, 2021. 2
- [27] Sourabh Vora, Alex H Lang, Bassam Helou, and Oscar Beijbom. PointPainting: Sequential Fusion for 3D Object Detection. In *CVPR*, pages 4604–4612, 2020. 2, 3, 4, 6
- [28] Tai Wang, Xinge Zhu, Jiangmiao Pang, and Dahua Lin. Fcos3d: Fully convolutional one-stage monocular 3d object detection. *arXiv preprint arXiv:2104.10956*, 2021. 2, 4, 6
- [29] Tai Wang, Xinge Zhu, Jiangmiao Pang, and Dahua Lin. Probabilistic and geometric depth: Detecting objects in perspective. *arXiv preprint arXiv:2107.14160*, 2021. 6
- [30] Yan Wang, Wei-Lun Chao, Divyansh Garg, Bharath Hariharan, Mark Campbell, and Kilian Q Weinberger. Pseudo-LiDAR from Visual Depth Estimation: Bridging the Gap in 3D Object Detection for Autonomous Driving. In *CVPR*, pages 8445–8453, 2019. 2
- [31] Yue Wang, Alireza Fathi, Abhijit Kundu, David A. Ross, Caroline Pantofaru, Thomas A. Funkhouser, and Justin M. Solomon. Pillar-based object detection for autonomous driving. In *The European Conference on Computer Vision (ECCV)*, 2020. 2
- [32] Yue Wang, Vitor Campagnolo Guizilini, Tianyuan Zhang, Yilun Wang, Hang Zhao, and Justin Solomon. Detr3d: 3d object detection from multi-view images via 3d-to-2d queries. In *5th Annual Conference on Robot Learning*, 2021. 2, 4, 5, 6
- [33] Yue Wang and Justin M. Solomon. Object dgcnn: 3d object detection using dynamic graphs. In *2021 Conference on Neural Information Processing Systems (NeurIPS)*, 2021. 2, 4, 5, 6
- [34] Yue Wang, Yongbin Sun, Ziwei Liu, Sanjay E Sarma, Michael M Bronstein, and Justin M Solomon. Dynamic graph cnn for learning on point clouds. *Acm Transactions On Graphics (tog)*, 38(5):1–12, 2019. 2
- [35] Zhixin Wang and Kui Jia. Frustum convnet: Sliding frustums to aggregate local point-wise features for amodal 3d object detection. In *2019 IEEE/RSJ International Conference on Intelligent Robots and Systems (IROS)*, pages 1742–1749. IEEE, 2019. 3
- [36] Zining Wang, Wei Zhan, and Masayoshi Tomizuka. Fusing bird’s eye view lidar point cloud and front view camera image for 3d object detection. In *2018 IEEE Intelligent Vehicles Symposium (IV)*, pages 1–6. IEEE, 2018. 2, 3
- [37] Yan Yan, Yuxing Mao, and Bo Li. SECOND: Sparsely Embedded Convolutional Detection. *Sensors*, 18(10):3337, 2018. 2, 4, 5
- [38] Tianwei Yin, Xingyi Zhou, and Philipp Krähenbühl. Center-based 3D Object Detection and Tracking. *arXiv preprint arXiv:2006.11275*, 2020. 2, 4, 5, 6
- [39] Tianwei Yin, Xingyi Zhou, and Philipp Krähenbühl. Multi-modal virtual point 3d detection. *NeurIPS*, 2021. 3
- [40] Xingyi Zhou, Dequan Wang, and Philipp Krähenbühl. Objects as Points. *arXiv preprint arXiv:1904.07850*, 2019. 6
- [41] Yin Zhou, Pei Sun, Yu Zhang, Dragomir Anguelov, Jiyang Gao, Tom Ouyang, James Guo, Jiquan Ngiam, and Vijay Vasudevan. End-to-end multi-view fusion for 3d object detection in LiDAR point clouds. In *The Conference on Robot Learning (CoRL)*, 2019. 2
- [42] Yin Zhou and Oncel Tuzel. VoxelNet: End-to-End Learning for Point Cloud Based 3D Object Detection. In *CVPR*, pages 4490–4499, 2018. 2, 4, 7
- [43] Benjin Zhu, Zhengkai Jiang, Xiangxin Zhou, Zeming Li, and Gang Yu. Class-balanced grouping and sampling for point cloud 3d object detection. *arXiv preprint arXiv:1908.09492*, 2019. 5
- [44] Xizhou Zhu, Weijie Su, Lewei Lu, Bin Li, Xiaogang Wang, and Jifeng Dai. Deformable detr: Deformable transformers for end-to-end object detection. *arXiv preprint arXiv:2010.04159*, 2020. 5

A. Supplement

A.1. Simulation of low-resolution LiDARs

We convert each point in point clouds from Cartesian coordinate system (x, y, z) to spherical coordinates (r, θ, ϕ) as

$$\begin{aligned} r &= \sqrt{x^2 + y^2 + z^2} \\ \theta &= \arcsin \frac{z}{\sqrt{x^2 + y^2 + z^2}} \\ \phi &= \arctan \frac{y}{x} \end{aligned} \quad (9)$$

We pick the points according to the pitch angle θ . The range of pitch angle in nuScenes is $[-30^\circ, 10^\circ]$, and the interval between adjacent beams is about 1.3° . For results in experiments, we select beams whose pitch angle θ fall within $[-7.1^\circ, -5.8^\circ] \cup [-4.5^\circ, -3.2^\circ] \cup [-1.9^\circ, -0.6^\circ] \cup [0.7^\circ, 2.0^\circ]$ as 4-beam LiDAR and the beam with pitch angle in $[-1.9^\circ, -0.6^\circ]$ as 1-beam LiDAR.

A.2. More results

A.2.1 Results with 16-beam LiDAR

16-beam LiDARs are also popular sensors in real-world applications. To simulate a 16-beam LiDAR, we select 16 beams evenly from the original 32 beams.

Table A. Results with 16-beam LiDAR.

	NDS	mAP
16-beam LiDAR	58.2	47.2
16-beam LiDAR + Cameras	63.4	57.7

A.2.2 Results on training jointly from scratch

In experiments, we pre-train the LiDAR backbone and the camera backbone respectively, then jointly fine-tune the model for the LiDAR-Camera model. When we train the LiDAR-Camera model jointly from scratch, the results are lower than pre-training by 6.0 mAP.

Table B. Comparing results on pre-training and from scratch.

	NDS	mAP
no pre-training	63.1	58.2
pre-training	68.0	64.2

A.2.3 Results with different beam choices

In the simulation of low-resolution LiDARs, we find the choices of LiDAR beams will affect the model performance.

We tried several beam combinations and report results in Table C and Table D.

Table C. Results on different beam choices in 1-beam LiDAR simulation.

	1-beam LiDAR		1-beam LiDAR + Cameras	
chosen beam	NDS	mAP	NDS	mAP
$[-0.6^\circ, 0.7^\circ]$	36.5	14.9	50.2	41.4
$[-1.9^\circ, -0.6^\circ]$	37.9	16.4	50.0	41.3
$[-3.2^\circ, -1.9^\circ]$	38.5	17.1	49.9	40.9
$[-4.5^\circ, -3.2^\circ]$	36.9	15.2	49.4	41.4
$[-5.8^\circ, -4.5^\circ]$	34.5	12.3	46.7	38.2
$[-7.1^\circ, -5.8^\circ]$	30.4	9.0	45.1	36.5

A.3. More visualizations

We visualize the results of FUTR3D with different configurations of input modalities in Fig A, Fig B and Fig C.

A.4. Use of existing assets

Codebase We use MMDetection3D [7] for baseline experiments and implementation of our own algorithms. MMDetection3D provides a solid implementation of a wide variety of 3D detection algorithms. MMDetection3D is licensed under Apache License, Version 2.0.

Dataset All of our experiments are carried out on the nuScenes [1] benchmark. The nuScenes dataset is licensed under a Creative Commons Attribution-NonCommercial-ShareAlike 4.0 International Public License (“CC BY-NC-SA 4.0”), with the additional terms listed in <https://www.nuscenes.org/terms-of-use>.

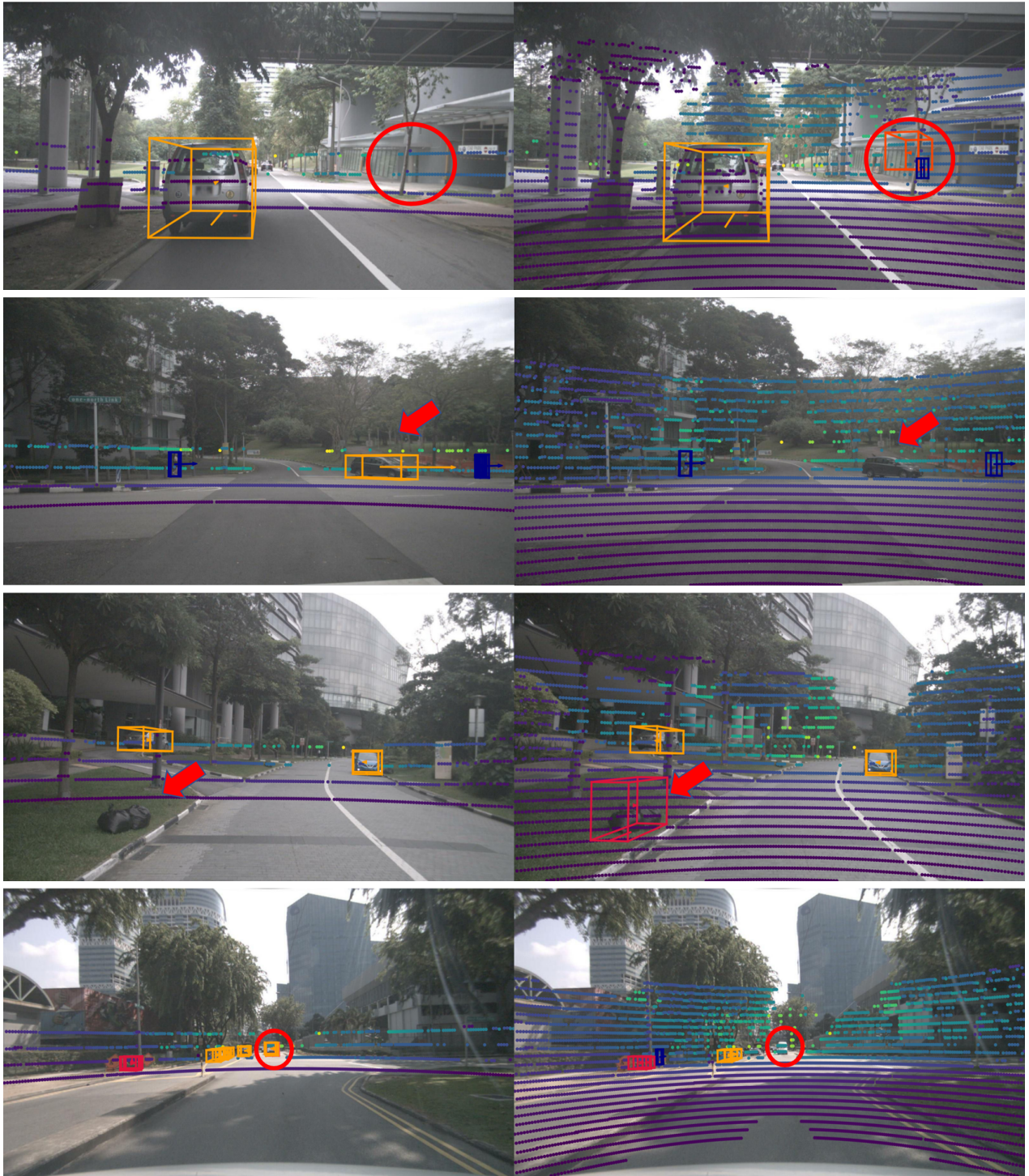


Figure A. Results visualization in perspective images. On the left is 4-beam LiDAR with cameras; on the right is 32-beam LiDAR. FUTR3D with 4-beam LiDAR with cameras achieves competitive performance compared to 32-beam LiDAR, especially for small objects like pedestrians and bicycles, and objects in the distance.



Figure B. Results visualization in perspective images. On the left is 1-beam LiDAR with cameras, on the right is cameras. Even sparse points like 1-beam LiDAR can help FUTR3D to detect and correct the false positive.

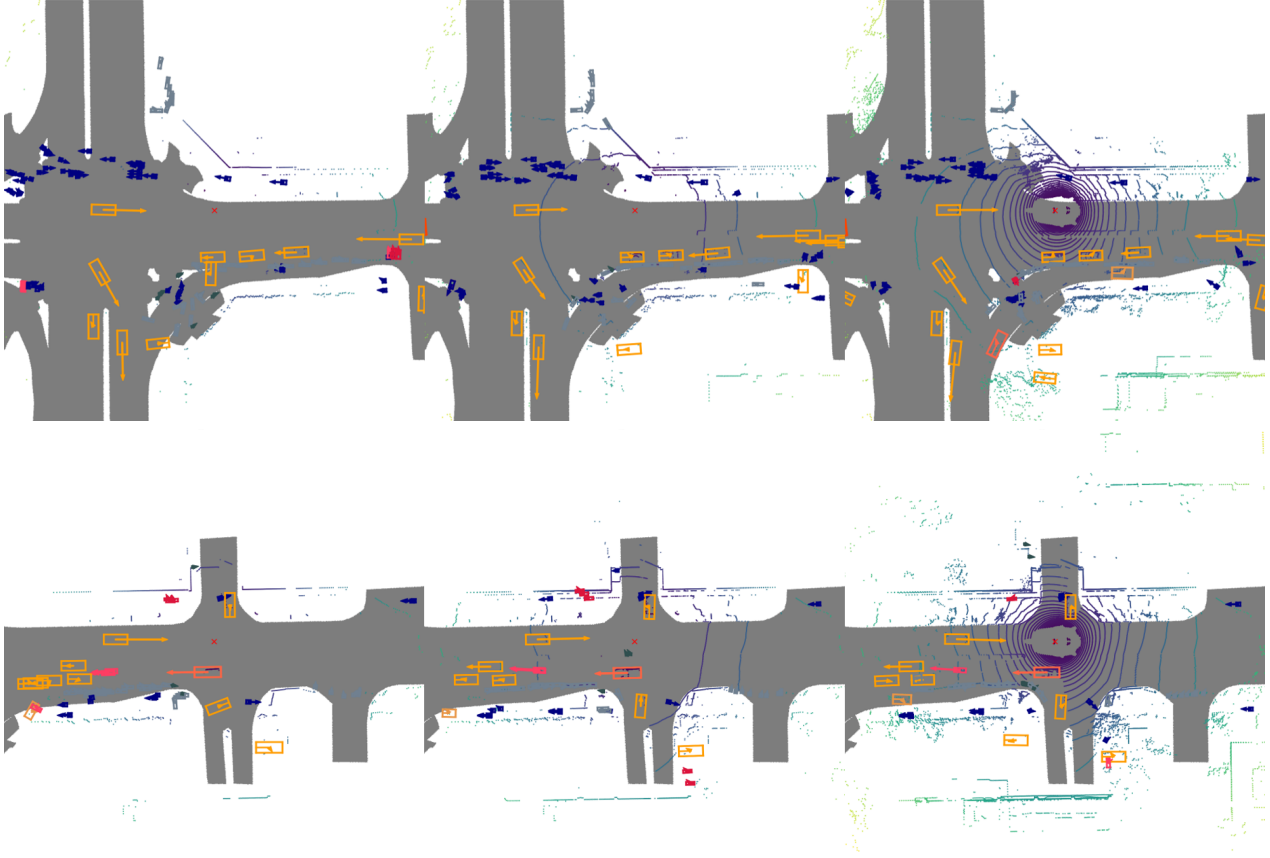


Figure C. Results visualization in BEV. On the left is 1-beam LiDAR with cameras, in the middle is 4-beam LiDAR with cameras and on the right is 32-beam LiDAR with cameras.

Table D. Results with 4-beam LiDAR simulation.

chosen beams	4-beam LiDAR		4-beam LiDAR+Cam	
	NDS	mAP	NDS	mAP
$[-4.5^\circ, -3.2^\circ] \cup [-3.2^\circ, -1.9^\circ] \cup [-1.9^\circ, -0.6^\circ] \cup [-0.6^\circ, 0.7^\circ]$	54.2	40.4	61.1	54.8
$[-3.2^\circ, -1.9^\circ] \cup [-1.9^\circ, -0.6^\circ] \cup [-0.6^\circ, 0.7^\circ] \cup [0.7^\circ, 2.0^\circ]$	52.1	37.5	59.8	52.4
$[-5.8^\circ, -4.5^\circ] \cup [-4.5^\circ, -3.2^\circ] \cup [-3.2^\circ, -1.9^\circ] \cup [-1.9^\circ, -0.6^\circ]$	52.8	38.1	59.4	51.9
$[-8.4^\circ, -7.1^\circ] \cup [-5.8^\circ, -4.5^\circ] \cup [-3.2^\circ, -1.9^\circ] \cup [-0.6^\circ, 0.7^\circ]$	54.0	40.4	61.3	54.3
$[-7.1^\circ, -5.8^\circ] \cup [-4.5^\circ, -3.2^\circ] \cup [-1.9^\circ, -0.6^\circ] \cup [0.7^\circ, 2.0^\circ]$	54.8	42.1	61.5	54.9